DAMAGE EVOLUTION OF VEHICLE MOTOR ROTOR UNDER SINGLE WORKING CONDITION BASED ON GTN MODEL

LIANGE HE

Key Laboratory of Advanced Manufacturing Technology for Automobile Parts, Chongqing University of Technology,
Ministry of Education, Chongqing, China; and

Key Laboratory of Modern Measurement and Control Technology, Ministry of Education, Beijing Information Science
and Technology University, Beijing, China; and

Chongqing Tsingshan Industrial Co., Ltd., Chongqing, China

e-mail: heliange@cqut.edu.cn

ZHOU YUAN, WENJUN SHI, XIANG QU

Key Laboratory of Advanced Manufacturing Technology for Automobile Parts, Chongqing University of Technology,
Ministry of Education, Chongqing, China

To study evolution of the void in the material of a motor rotor under different working conditions from a mesoscopic perspective, damage analysis of the rotor has been carried out based on thermal-mechanical coupling theory. According to the test methods of GB/T 228.1-2010 Part 1 and GB/T 228.2-2015 Part 2, tensile tests were conducted on rotor materials at different temperatures to obtain basic mechanical property parameters, and parameters of the fine-scale damage model at different temperatures were fitted by combining orthogonal tests and a finite element inverse calibration method. Then, the accurate temperature distribution law of the motor rotor was obtained through CFD calculation. Based on the material parameters and temperature data, the void evolution of the rotor material under thermal-mechanical load was studied by using the finite element method. The results show that: under the rated conditions, the stress concentration of the rotor is mainly appeared in the joint with the shaft, the maximum stress was 304.1 MPa, which did not reach the yield limit of the material. No plastic deformation occurred, so the volume fraction of voids inside the rotor material did not change still for the initial pore volume fraction of $2.5 \cdot 10^{-3}$. In the peak condition, the stress concentration appeared in the rotor plate across the joint of the magnetic bridge and pole shoe with a maximum stress of 354.4 MPa and a small plastic strain of $1.133 \cdot 10^{-3}$. The pore volume fraction increased to $2.503 \cdot 10^{-3}$, where the initial pore growth of $2.150 \cdot 10^{-6}$ and the secondary pore nucleation of $2.079 \cdot 10^{-12}$.

Keywords: motor rotor, GTN model, parameter fitting, void evolution

1. Introduction

The permanent magnet synchronous motor has a broad application prospect in the field of electric vehicles because of its small size, high power density, direct drive and high transmission efficiency (Gerada *et al.*, 2013; He and Shi, 2020; Ahn *et al.*, 2017; Xu *et al.*, 2019) but it also has defects. The rotor magnet steel has high compressive strength but low tensile strength. With an increase of speed, the rotor and permanent magnet generate a centrifugal force, and a too big centrifugal force may damage the rotor and affect safe operation of the permanent magnet synchronous motor (Tenconi *et al.*, 2013; Liu *et al.*, 2021; Zhu *et al.*, 2021; Zhang *et al.*, 2016).

The strength of rotors of the automotive permanent magnet synchronous motor has been widely researched (Shao *et al.*, 2019; Zhang *et al.*, 2017), and the main research methods focused on the analytical and finite element methods. The analytical method has advantages of easy

calculation, high efficiency, and being suitable for the optimal design of rotor strength. But derivation of the analytical solution is difficult, especially for a complex structure of the rotor, while the finite element method has high accuracy, but difficult modeling and large calculation. One of the more classic analytical methods is the equivalent circular method proposed by Binder *et al.* (2005), quick in calculation, but only applicable to most of simple structures of high-speed motors.

It is difficult to consider a variety of loads comprehensively. Li *et al.* (2014) improved the equivalent circular method to make calculations more accurate. Feng *et al.* (2016) not only improved the equivalent circular method to enhance calculation accuracy, but also proposed analytical calculation of the V-shaped rotor, and the results obtained from the analytical algorithm were verified by the finite element method. Although the analytical method fully reflects the advantages of fast calculation, it can only solve some objects with relatively regular geometry and has very limited applications, so researchers mainly use the finite element method in analysis of rotor strength of automotive permanent magnet synchronous motors. Gao *et al.* (2021) conducted an in-depth study on the rotor strength problem and structural design method of a high-speed permanent magnet motor, and established a calculation model that can consider mechanical overload, temperature rise and centrifugal force at the same time. They also used the finite element method to study stress distribution characteristics and change the law of rotor structure under different working conditions. From the aspect of thermal-structural coupling, Liang *et al.* (2011) used the 3D finite unit method to analyze coupled electromagnetic and centrifugal forces in the rotor of a permanent magnet motor and obtained an accurate 3D stress distribution in the rotor. Xie *et al.* (2019) established analytical equations and a multi--objective optimization model for the problem of the spacer bridge which is easily damaged under the centrifugal force of a high-speed V-shaped built-in rotor and found the optimal design and structural parameters of the permanent magnet rotor. In conclusion, whether from an analytical or finite element method, the strength of the rotor is studied based on the traditional strength theory.

To study the effect of nucleation and growth of micro-pores within the material on mechanical properties of the material on a mesoscale level, the Gurson-Tvergaard-Needleman damage model (GTN) was introduced to describe the development of tiny defects within the material. The GTN model was pioneered by Gurson (1977) as a more complete damage intrinsic model, which was later supplemented by Tvergaard and Needlemann (1984) and Needleman and Tvergaard (1984) where three coefficients were introduced by considering the interaction of pores inside the material. A more mature GTN intrinsic model was obtained after modification. Li and Cui (2020) studied the toughness damage and damage evolution of aluminum alloy materials based on the GTN model. Sun *et al.* (2013) predicted the direction of edge crack sprouting and expansion during cold rolling of silicon steel plates. Fang *et al.* (2020) showed that the initial hole volume, by using the GTN model for crack expansion fraction, has a large influence on the prediction results of the GTN model. Mobasher *et al.* (2022) and Dong *et al.* (2021) based on the GTN model with shear correction accurately predicted the crack extension during pipe shearing. Lee *et al.* (2022) modified the GTN model by Hershey Hosford's non-quadratic isotropic plastic yield criterion, and better predicted the plastic and ductile damage behavior of 2024-O aluminum alloy.

Although researchers have done a lot of studies on strength of motor rotors, they mostly start from the macroscopic structure of the rotor, analyze stress distribution characteristics of the rotor under different operating conditions, and improve the stress concentration by optimizing the rotor structure. They all start from the traditional strength theory and cannot fundamentally describe the damage evolution process of materials (including micro-porosity, micro-cracks, impurities, etc.) during plastic deformation without considering the relationship between the physical mechanism of damage generation and microstructure evolution inside the

material. The research on damage evolution of rotor silicon steel materials is currently concentrated at room temperature, and less research has been done at high temperatures. Yan *et al.* (2013) used the GTN model to investigate the damage distribution as well as crack sprouting and extension in silicon steel plates with tiny notches on the edges during cold rolling. Nioi *et al.* (2019) developed a finite element model to simulate the evolution of surface defects in high-Si electrical steel under one-pass hot rolling operation. However, due to the working environment of the motor rotor, high-temperature mechanical properties of a non-oriented silicon steel sheet used in it determine the level of high-temperature resistance and service-bearing strength of the rotor.

Therefore, to obtain mechanical parameters of silicon steel at each temperature, tensile tests were conducted at room temperature, 70°C, 100°C and 150°C. Parameters of the GTN damage model at each temperature of silicon steel were determined by the finite element inverse calibration method, and then the accurate temperature distribution law of the motor rotor was obtained by CFD calculation. Then, based on the material parameters and temperature data, the finite element method was used to study the hole evolution law of the rotor material under thermal-mechanical load, in the hope that it will provide some reference to design and development of a high-speed vehicle drive motor.

2. GTN damage model

In the modified Gurson-Tvergaard-Needleman (GTN) model, the yield function has the following form

$$\phi = \frac{\sigma_{eq}}{\overline{\sigma}_m} + 2f^* q_1 \cosh \frac{3q_2 \sigma_h}{2\overline{\sigma}_m} - \left(1 + q_3 f^{*2}\right) = 0 \tag{2.1}$$

where σ_{eq} is the equivalent stress, σ_h is the hydrostatic stress, $\overline{\sigma}_m$ is the yield stress, q_1, q_2, q_3 are damage parameters considering the interaction between pores, f^* is the equivalent pore volume fraction, the following expression can be used

$$f^* = \begin{cases} f & \text{for} \quad f \leqslant f_c \\ f_c + k(f - f_c) & \text{for} \quad f > f_c \end{cases} \quad \text{and} \quad k = \frac{f_u - f_c}{f_f - f_c} \tag{2.2}$$

where f is the void volume fraction, k is the acceleration factor, f_c is the volume fraction when pores are aggregated, f_f is the volume fraction at material fracture, f_u is the void volume fraction when the stress drops to 0, $f_u = 1/q_1$.

For porous metal materials, the equivalent plastic strain in the matrix material can be obtained by the equivalent plastic work which is expressed as

$$(1 - f)\overline{\sigma}_m d\overline{\varepsilon}^{pl} = \sigma d\varepsilon^{pl} \tag{2.3}$$

where $d\overline{\varepsilon}^{pl}$ is the equivalent plastic strain increment, $d\varepsilon^{pl}$ is the plastic strain increment.

The increase in the volume fraction of pores, on one hand is the growth of existing pores, on the other hand, the nucleation of the grown pores into new pores

$$df = df_{growth} + df_{nucleation} \tag{2.4}$$

where df_{growth} represents the change in volume fraction when the existing pores grow up, $df_{nucleation}$ represents the change in volume fraction when the pores nucleate, and they are governed by the law of conservation of mass

$$df_{growth} = (1 - f)d\varepsilon^{pl} : \mathbf{I} \qquad df_{nucleation} = A d\overline{\varepsilon}^{pl} \tag{2.5}$$

and

$$A = \frac{f_n}{S_n\sqrt{2\pi}} \exp\Big[-\frac{1}{2}\Big(\frac{\overline{\varepsilon}^{pl} - \varepsilon_n}{S_n}\Big)^2\Big] \tag{2.6}$$

where $\mathbf{I}$ is the second-order unit tensor, S_n is the standard deviation of nucleation, ε_n is the average equivalent plastic strain of nucleation, and f_n is the percentage of nucleation void volume.

3. Identification of silicone steel GTN damage parameters

3.1. Identification of GTN damage parameters at room temperature

3.1.1. Material tensile test

To obtain mechanical properties of silicon steel materials, it is necessary to conduct a one-way tensile test on a material specimen. The chemical composition of the test materials is shown in Table 1.

Table 1. Chemical composition of test materials (% in weight)

C	Si	Mn	P	S	Ti	V
0.016	1.997	0.243	0.131	0.015	0.014	0.018

This test uses national standard GB/T228.1-2010 tensile test of metal materials, Part 1: Room temperature test method. The dimensions of the tensile specimen are shown in Fig. 1. INSTRON company in the United States produced a universal material testing machine for uniaxial tensile tests with tensile speeds of 1 mm/min.
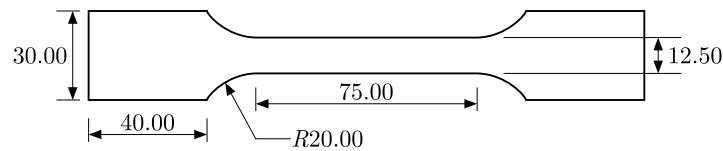

Fig. 1. Tensile specimen at room temperature

The nominal stress-strain curve shown in Fig. 2 was obtained by fitting the test data after the test was completed.

The mechanical properties of silicon steel were obtained, as shown in Table 2.

Table 2. Mechanical properties of silicon steel at room temperature

Material	E [GPa]	$\sigma_{0.2}$ [MPa]	R_m [MPa]	ν
Silicon	180	405	513	0.30

The stress and strain in the nominal stress-strain curve mentioned above are calculated from the initial size of the sample. In fact, the size of the sample is constantly changing during the test, so the true strain ε_{true} and true stress σ_{true} need to be obtained through calculation of the nominal strain ε_{nom} and nominal stress σ_{nom} to fit the true stress-strain curve, as is shown in Fig. 2. They can be converted by the following formula

$$\varepsilon_{true} = \int_{l_0}^{l} \frac{1}{l}\,dl = \ln\frac{l}{l_0} = \ln(1 + \varepsilon_{nom})$$

$$\sigma_{true} = \frac{F}{A} = \frac{F}{A} = \frac{F}{A_0\frac{l}{l_0}} = \sigma_{nom}(1 + \varepsilon_{nom}) \tag{3.1}$$

where l is the current length of the sample, l_0 is its initial length, A is the current area, A_0 is the initial area of the sample, F is the applied load.

The true strain consists of elastic and plastic strain, so when defining plasticity in the finite element calculation software, the plastic strain value needs to be calculated with the following formula

$$\varepsilon_p = \varepsilon_{true} - \varepsilon_e = \varepsilon_{rrue} - \frac{\sigma_{true}}{E} \tag{3.2}$$

where E is the modulus of elasticity.
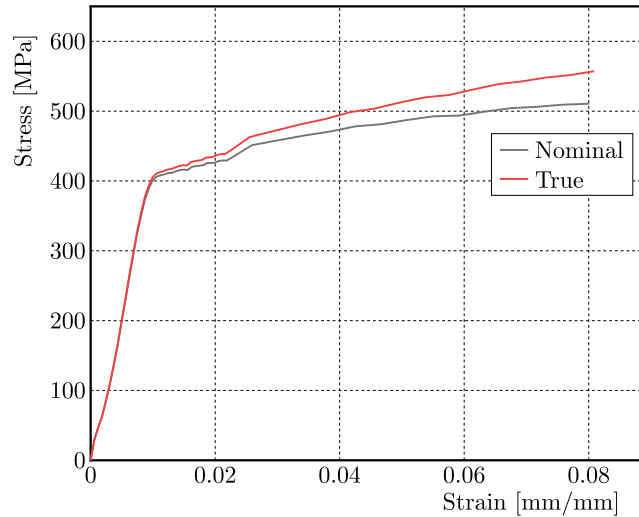
Fig. 2. True stress-strain curves of silicon steel

3.1.2. Damage parameter identification

For nine parameters of the GTN damage model, where the correction coefficients q_1, q_2 and q_3 are related to the matrix reinforcement material, Tvergaard and Needleman (1984) showed that when $q_1 = 1.5$, $q_2 = 1$ and $q_3 = q_1^2$, the results are most suitable for calculation of the body cell model for metallic materials. f_0, f_c and f_f are obtained by using scanning electron microscope (SEM) observations. $f_0 = 0.0025$, $f_c = 0.101$ and $f_f = 0.155$ are quoted here from SEM observations of a thin silicon steel plate by Sun *et al.* (2013). The three parameters ε_n, S_n and f_n are given as recommended values based on extensive experiments by researchers, and for metallic materials at room temperature they are $\varepsilon_n = 0.1 \sim 0.3$, $S_n = 0.05 \sim 0.1$ and $f_n = 0.01 \sim 0.04$ (Huang, 2016).

To reduce the computational cost, an orthogonal experimental design method was used for three parameters ε_n, S_n and f_n, with 3 levels for each parameter in the range and 3 parameters for the study, i.e., 3 factors and 3 levels. And without considering the interaction between the factors, the experimental scheme was obtained as shown in Table 3.

The finite element model was established according to the tensile test in Section 3.1.1, finite element simulations were performed for all the test scenarios in Table 2, and the comparative results shown in Fig. 3 were obtained after compiling the data.

By comparing the test and simulation results, it is found that the simulation results of test No. 3 are closest to the test results, so the GTN fine damage parameters of the silicon steel material at room temperature can be obtained, as shown in Table 4.

Table 3. Orthogonal test scheme

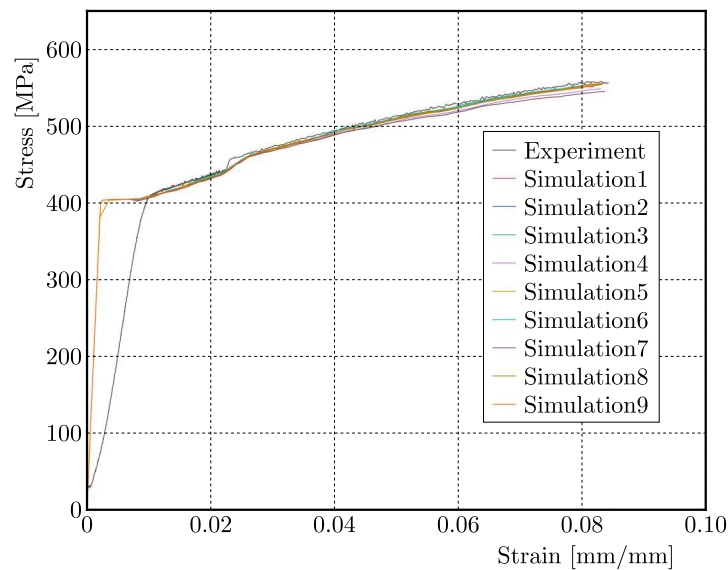| Number	ε_n	S_n	f_n
1	0.1	0.05	0.01
2	0.2	0.075	0.01
3	0.3	0.1	0.01
4	0.1	0.075	0.0025
5	0.2	0.1	0.0025
6	0.3	0.05	0.0025
7	0.1	0.1	0.04
8	0.2	0.05	0.04
9	0.3	0.075	0.04

Fig. 3. Comparison of stress-strain curves between test and simulation results

Table 4. Damage parameters of the GTN model at room temperature

q_1	q_2	q_3	f_0	f_c	f_f	ε_n	S_n	f_n
1.5	1.0	2.25	0.0025	0.101	0.155	0.3	0.1	0.01

3.2. Identification of GTN damage parameters at high temperature

3.2.1. High temperature tensile test

A high-temperature tensile test and preparation of high-temperature tensile specimens refer to GB/T 228.2-2015 tensile test of metal materials standard Part 2: High-temperature test method. The test dimensions are shown in Fig. 4, where: $b_0 = 12.5$ mm, head length $C = 50$ mm, head width $B = 35$ mm, hole diameter $D = 15$ mm, transition $R = 25$ mm, parallel section length $l_c = 62.5$ mm, thickness of 2 mm. The tensile speed is the same as in the room temperature tensile test, but the temperatures are 70°C, 100°C and 150°C.

The yield strength and tensile strength at each temperature were obtained from tests as shown in Table 5.

As in the material tensile test, the data were extracted after the test was completed and true stress-strain curves were obtained by fitting according to Eqs. (3.1). The stress-strain curves of the silicon steel material at 70°C, 100°C and 150°C are shown in Fig. 5.
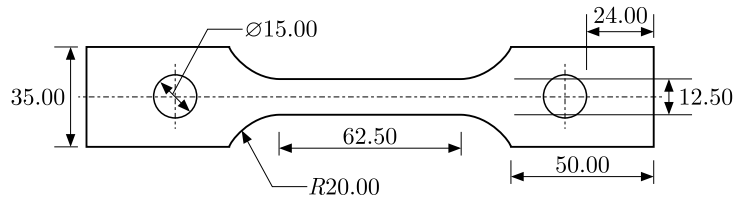
Fig. 4. Uniaxial tensile specimen at high temperature

Table 5. Yield strength and tensile strength of materials at three temperatures

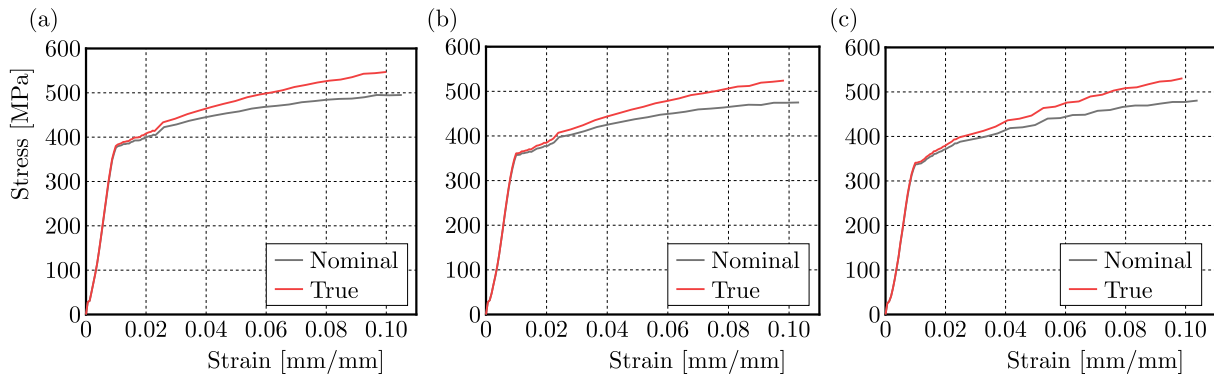| Parameters	Temperature		
	70°C	100°C	150°C
E [GPa]	176	175	173
$\sigma_{0.2}$ [MPa]	375	354	337
R_m [MPa]	495	476	480

Fig. 5. Stress-strain curves at three different temperatures: (a) 70°C, (b) 100°C, (c) 150°C

Table 6. The coefficient of thermal expansion (CTE) of silicon steel materials at different temperatures

Temperatures [^{c}ircC]	CTE [$(1/k) \cdot 10^{-5}$]
70	1.758
100	1.524
150	1.402

The coefficient of thermal expansion (CTE) of silicon steel materials at different temperatures is given in Table 6.

3.2.2. Influence of nucleation parameters on finite element simulation

In the GTN model, the temperature-dependent damage parameters are mainly three nucleation parameters: the average equivalent plastic strain ε_n, the standard deviation of nucleation strain S_n, and the volume fraction of nucleation holes f_n. The following three parameters are used to study the effect of parameter variations on the mechanical properties of silicon steel materials, and to adjust these parameters so that the stress-strain curves obtained from finite element calculations at each temperature are as close as possible to the test curves at each temperature.

Due to space limitation, we take the average equivalent plastic strain ε_n as an example and adopt the same treatment method for the standard deviation of nucleation strain S_n and the volume fraction of nucleation holes f_n.

Then we use the ε_n parameter values obtained in Section 3.1.2 at room temperature as the reference values, considering a fluctuation range of 50% and keeping the remaining 8 parameters constant by default.

Table 7. GTN damage parameters for different ε_n

q_1	q_2	q_3	f_0	f_c	f_f	ε_n	S_n	f_n
						0.15		
1.5	1	2.25	0.0025	0.101	0.155	0.3	0.1	0.01
						0.45		

After finite element calculation, the stress-strain curves were obtained for different n, and the comparison with the experimental results is shown in Fig. 6.
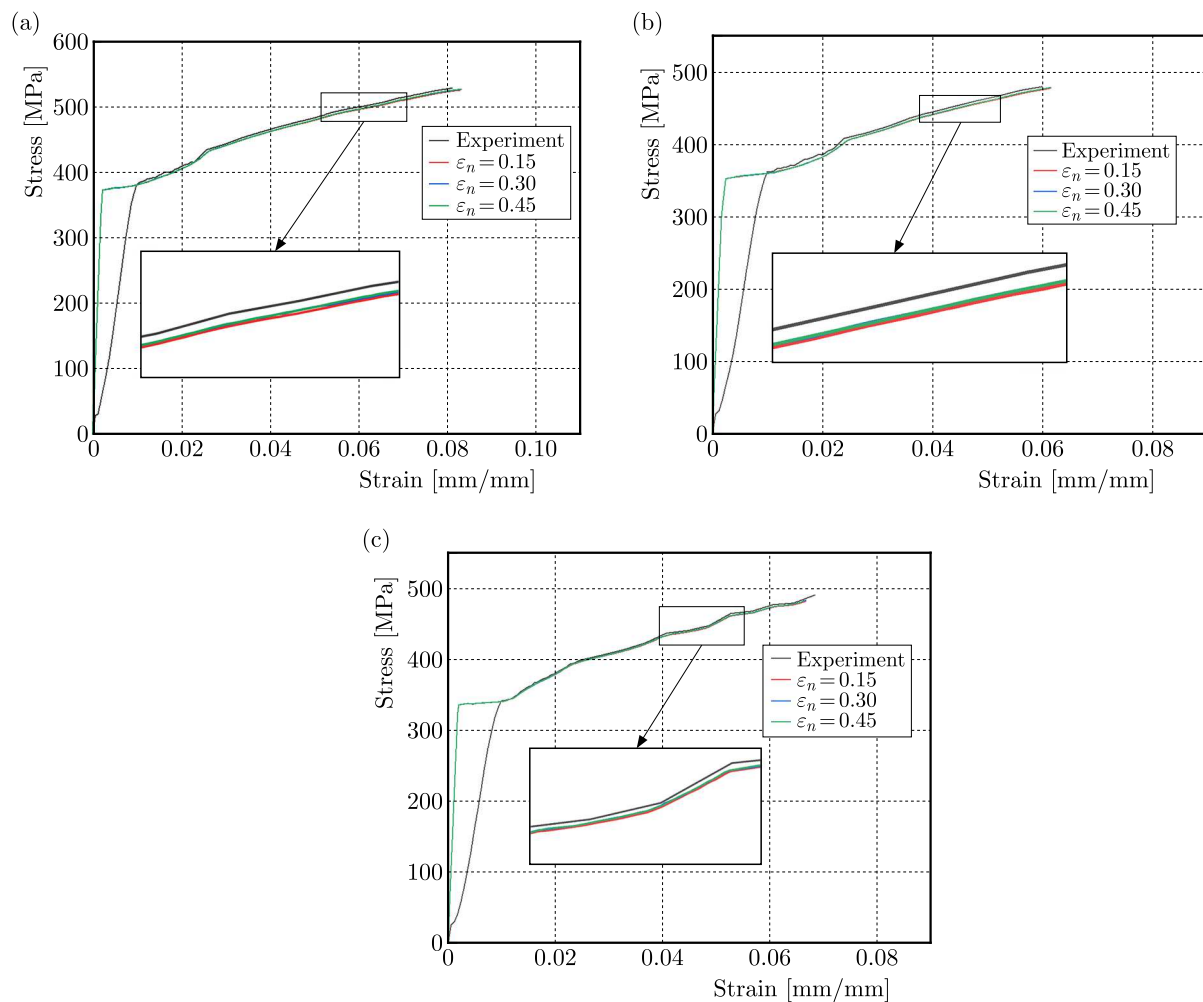
Fig. 6. Comparison between stress-strain curves of different ε_n and experiments: (a) 70°C, (b) 100°C, (c) 150°C

As can be seen in Fig. 6, with $\varepsilon_n = 0.3$ as the reference value, the effect of the average equivalent plastic strain ε_n on the mechanical properties of the silicon steel material at the three temperatures shows consistency, i.e., when ε_n increases, the finite element calculation

results approach upward the experimental to curve, while when ε_n decreases, the finite element calculations show almost no change.

For the standard deviation of nucleation strain S_n and the volume fraction of nucleation holes f_n, when S_n decreases, the finite element calculation results move upward and approach the test curve, but the change of f_n has no significant influence on the mechanical properties of the silicon steel material.

3.2.3. *Determination of damage parameters at high temperatures*

From the analysis in Section 3.2.2, it can be seen that the increasing ε_n and decreasing S_n can make the finite element calculation results closer to the experimental results, while the change of f_n has little effect on the mechanical properties of the material, so the values of f_n at 70°C, 100°C and 150°C are still kept the same as those at room temperature, i.e., $f_n = 0.01$.

After a series of trial calculations according to the above rule, the final three sets of GTN damage parameters were obtained in good agreement with the experiment curves at the three temperatures, see Fig. 7.
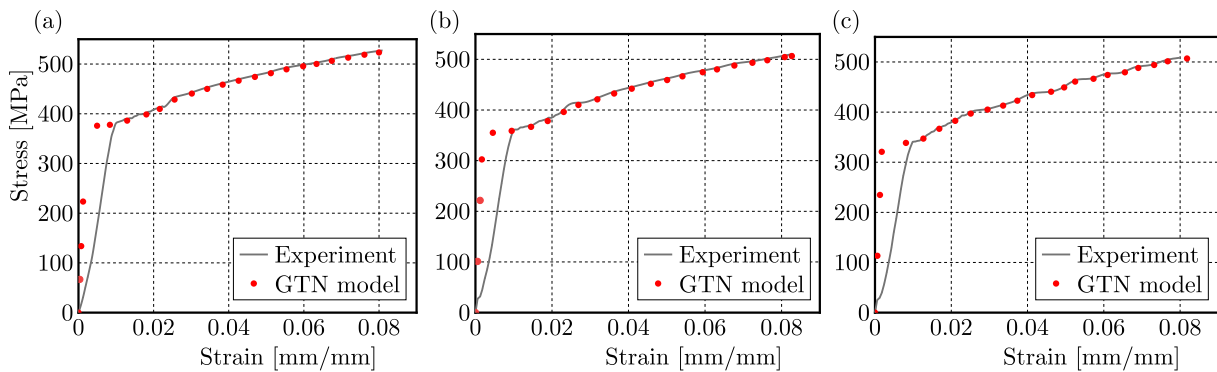
Fig. 7. Fitting results of parameters at different temperatures: (a) 70°C, (b) 100°C, (c) 150°C

From Fig. 7, it can be seen that the mechanical properties of the silicon steel specimens calculated by the GTN model are in good agreement with the experiment curves, so the damage parameters of the GTN model at room temperature, 70°C, 100°C and 150°C are obtained and given in Table 8.

Table 8. The damage parameters of the GTN model

Temperature	Parameters								
	q_1	q_2	q_3	f_0	f_c	f_f	ε_n	S_n	f_n
Room	1.5	1	2.25	0.0025	0.101	0.155	0.3	0.1	0.01
70°C	1.5	1	2.25	0.0025	0.101	0.155	0.33	0.08	0.01
100°C	1.5	1	2.25	0.0025	0.101	0.155	0.35	0.06	0.01
150°C	1.5	1	2.25	0.0025	0.101	0.155	0.37	0.05	0.01

4. Mesoscopic damage study of the rotor of the motor

4.1. Determination of rotor temperature for rated and peak operating conditions

To verify the accuracy of the simulation process and results, experiments and simulations were carried out on the prototype with the basic parameters shown in Table 9. A temperature rise test platform has been built as shown in Fig. 8, which mainly included the motor under

test, dynamometer, new energy battery simulator, constant temperature water tank and a data acquisition system. The torque corresponding to different working conditions is input to the dynamometer as the load of the electric drive system under test, and the temperature of the water inlet is controlled by a constant temperature water tank to cool the electric drive system. The temperature of the motor is measured by embedding a thermocouple at the end of the prototype winding. To ensure timeliness and consistency of the data, the data acquisition system collects real-time temperature recordings.

Table 9. Basic parameters of the prototype

Parameter	Value	Parameter	Value
Stator outer diameter [mm]	145	Rated voltage [V]	350
Stator inner diameter [mm]	90	Rated power [kW]	20.7
Core length [mm]	100	Peak power [kW]	45
Rotor outer diameter [mm]	89	Rated speed [rpm]	4300
Rotor inner diameter [mm]	36	Peak speed [rpm]	15000
Number of slots	8	Rated torque [Nm]	46
Number of poles	48	Peak torque [Nm]	107
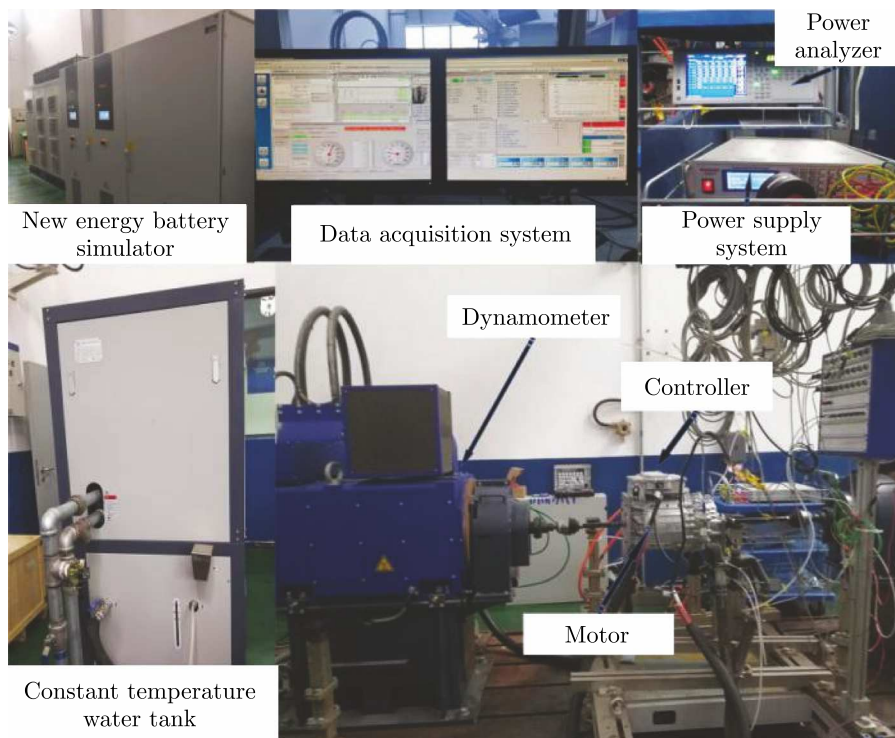
Fig. 8. Driving motor temperature rise test bench

Since it is difficult to measure the rotor temperature accurately, the accuracy of calculation of the rotor temperature of the motor is indirectly proved by measuring the winding temperature. The calculation method and process for the motor temperature have been described in detail in the literature (He *et al.*, 2021). The simulated temperature under two working conditions is compared with the temperature obtained from the test, and Fig. 9 is obtained. Under the rated working conditions, the temperature of the test prototype rises rapidly in the first 400 s and then tends to be stable after it slowly rises from 400 s to 1200 s. Although there is still a small increase in the follow-up, the temperature change does not exceed 1°C within 10 minutes, and the final temperature is 116°C. The temperature of the simulation is 116.4°C after running for 1800 s, and

the error is only 0.4°C. Under the peak condition, the winding temperature of the test prototype reaches 150°C at 228 s, and the winding temperature calculated by simulation reaches 150°C at 208 s. Comparing the time to reach the limit temperature, the difference between the simulation and the test is 20 s, and the relative error is 8.8%. Through comparison, it is found that the test and simulation results of the winding temperature under rated and peak conditions are within the allowable error range, and the temperature change trend is consistent, which verifies the accuracy of the motor temperature rise simulation calculation model.
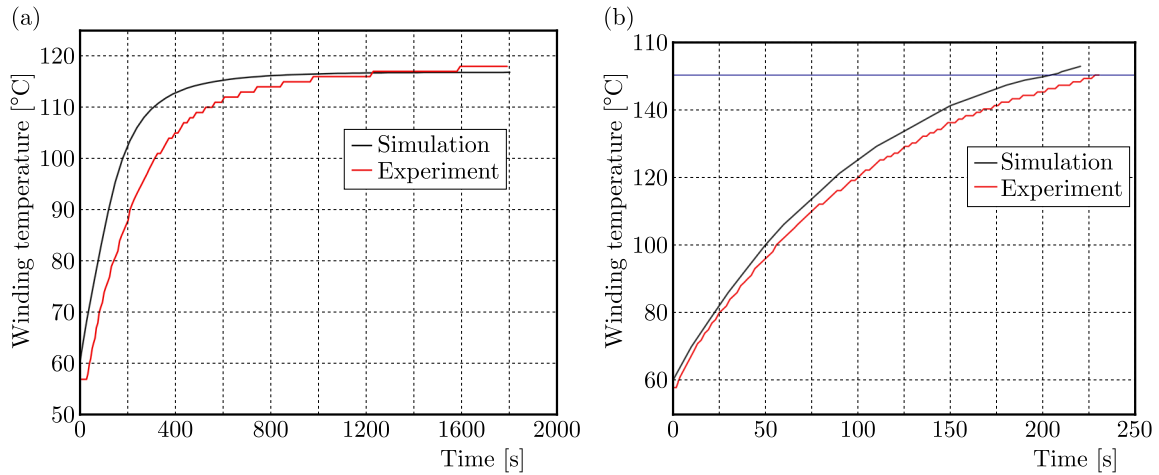
Fig. 9. Temperature comparison of winding: (a) rated operating condition, (b) peak working condition

The cloud diagrams of the rotor temperature distribution under the two working conditions are obtained by calculation, as shown in Fig. 10. The temperature distributions under the two working conditions are roughly the same, showing the phenomenon that the internal temperature is low and the external degree is high. Under the rated conditions, the maximum temperature of the rotor is 91.9°C, and the maximum temperature difference is 7.3°C. Under the peak working condition, because the rotor generates less heat, the heat accumulation is slow and the running time is short. The maximum temperature of the rotor is 91.3°C, which is lower than that under the rated working condition, and the maximum temperature difference is 34.6°C, which is significantly higher than that under the rated working condition.
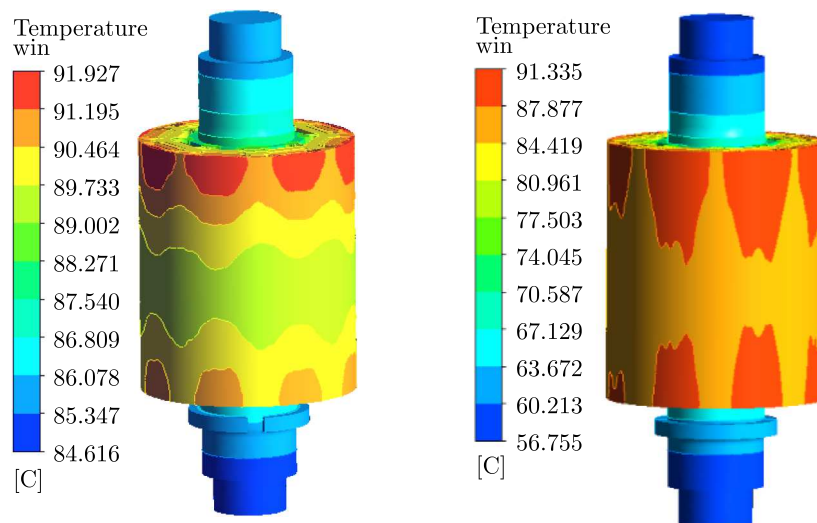
Fig. 10. Temperature distribution of the rotor: (a) rated operating condition, (b) peak working condition

4.2. Boundary condition setting

The simulation software used in this paper is ABAQUS, the interaction type between the outer surface of the shaft and the inner surface of the rotor is set to be surface-to-surface contact, and it is assumed that the contact surfaces are in a small sliding state between them, which satisfies the tangential friction condition of the small sliding state of Coulomb's theorem. Coulomb's friction jump-in is constrained using a penalty function, and the friction coefficient of the two surfaces is set to 0.15. The shaft and rotor are assembled with an interference, and the interference amount is set to 0.01. The tie constraint is used between the permanent magnet and the rotor. It limits the axial movement on both ends of the rotor; limits any displacement and rotation at the bearing mounting except for rotation around the shaft, and applies the centrifugal force to both the shaft and the rotor. The number of finite elements is 33672 and the shape is hexahedral.

4.3. Internal void evolution in the rotor material

To study the evolutionary behavior of the holes inside the rotor material under rated and peak operating conditions of the motor rotor, the rotor temperature field obtained in Section 4.1 is introduced into the finite element model, and a speed of $4300\,\mathrm{r/min}$ for rated operating conditions and $15000\,\mathrm{r/min}$ for peak operating conditions are applied.

When the motor is running under rated working conditions, the rotor and shaft adopt an interference fit, and the centrifugal force generated by rotation at $4300\,\mathrm{r/min}$ is not enough to offset the preload force due to the interference fit, so the stress concentration appears at the connection between the rotor and shaft, as shown in Fig. 11. At this time, the maximum stress
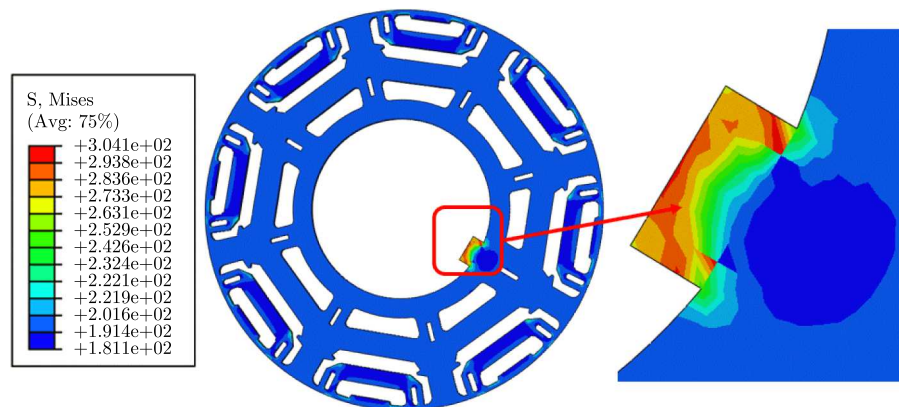

Fig. 11. Rotor stress cloud diagram at the rated working condition

is $304.1\,\mathrm{MPa}$, which does not reach the yield limit of the material. The elastic strain of the rotor is shown in Fig. 12, and the plastic strain is 0, i.e. the rotor is not plastically deformed.

Since the material itself has a small number of primary pores and second phase particles. This original defect is considered to be the initial pore inside the material, and it is known from Section 3.1.2 that the initial pore volume fraction of the silicon steel material is $f_0 = 2.5 \cdot 10^{-3}$. According to GTN principal equation (2.1), it is known that the change of pores inside the material is caused by plastic deformation of the material, and under the rated condition, the rotor is subjected to thermo-mechanical coupling stress that does not reach the yield limit of the material. The initial pores inside the rotor material do not grow and do not have new pore nuclei, and the pore volume fraction of the rotor is still equal to the initial pore volume fraction, as shown in Fig. 13.

When the motor is in the peak condition, the rotor speed will rise to $15000\,\mathrm{r/min}$ and the centrifugal force acting on the rotor will increase further, while the stress concentration
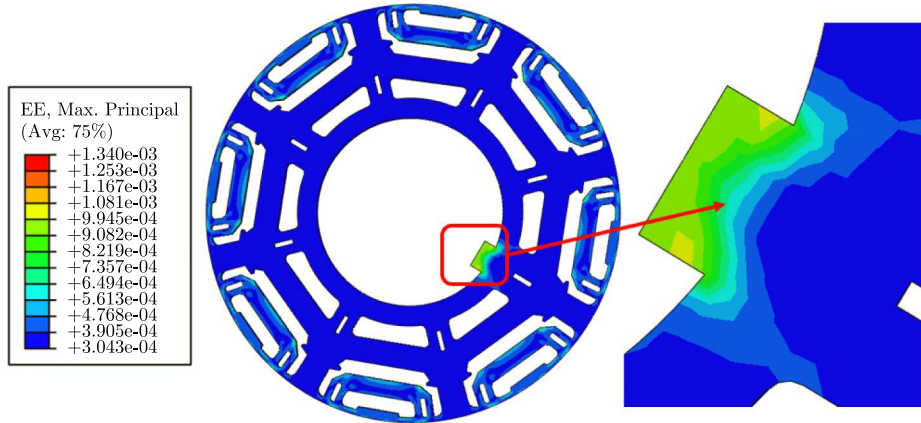
Fig. 12. Cloud diagram of rotor elastic strain at the rated working condition
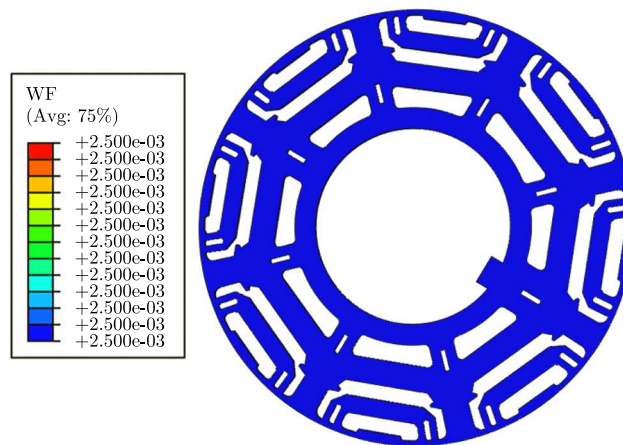

Fig. 13. Volume fraction of the rotor hole in the rated condition

between the rotor and the shaft due to the interference assembly will gradually decrease with an increase in the centrifugal force. Due to the centrifugal force of the permanent magnet, the stress concentration of the rotor will appear at the connection between the rotor punch plate spacer and the pole shoe, which is also the easiest part of the built-in rotor structure to break. The specific stress distribution is shown in Fig. 14, the maximum stress is 354.4 MPa.
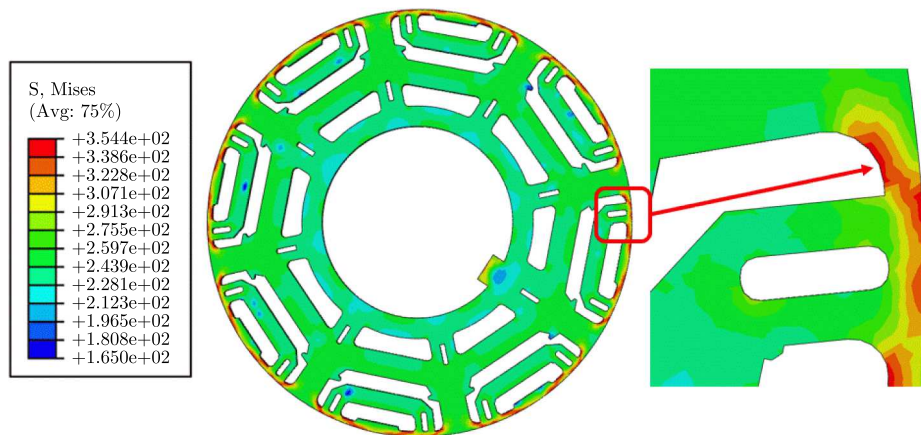
Fig. 14. Cloud diagram of the rotor stress distribution under the peak working condition
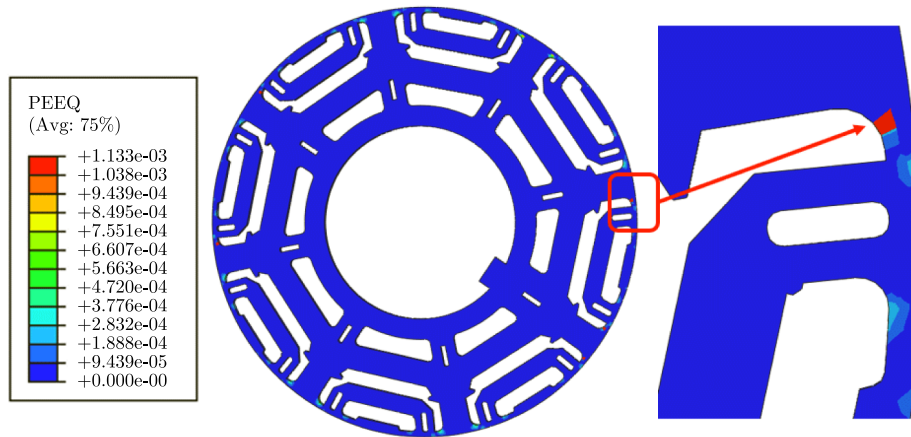
Fig. 15. Cloud diagram of the equivalent plastic strain of the rotor under the peak condition

When there is a significant increase in the local stress-strain level in the material or component, the microstructure inside the material also changes. As shown in Fig. 15, not only a high stress concentration but also some plastic deformation occurs at the connection between the rotor punch bridge and the pole shoe. The initial hole grows gradually under the effect of increasing stress (Fig. 16), resulting in the softening of the matrix around the hole and thus inducing the nucleation of secondary holes.
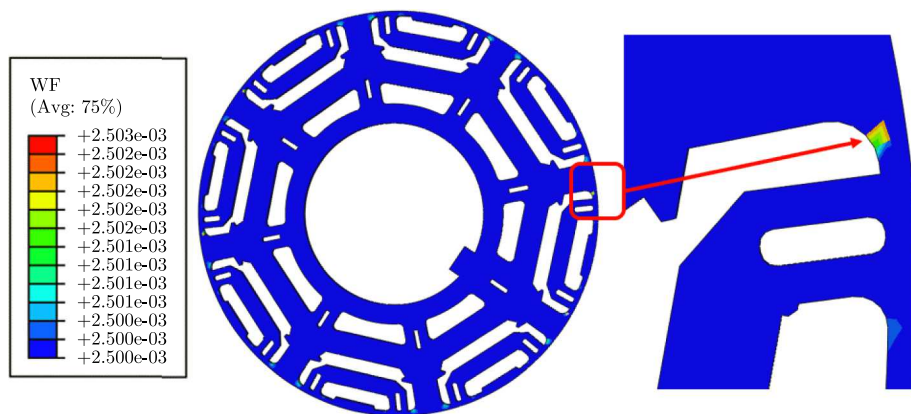
Fig. 16. Volume fraction of the rotor hole under the peak condition
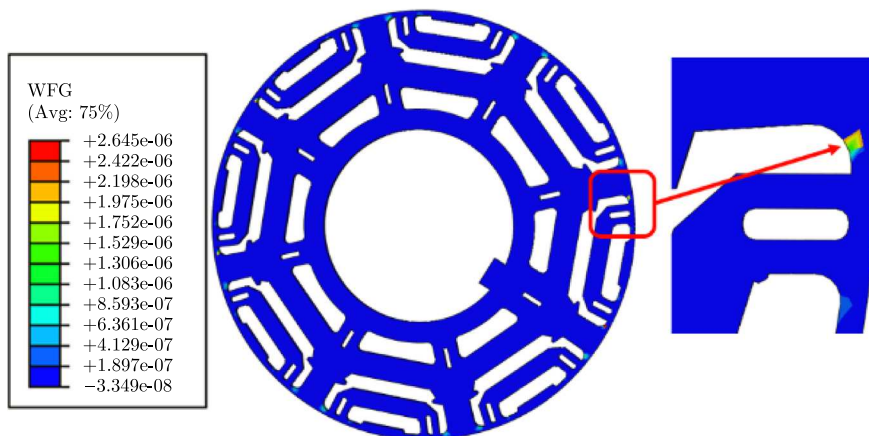

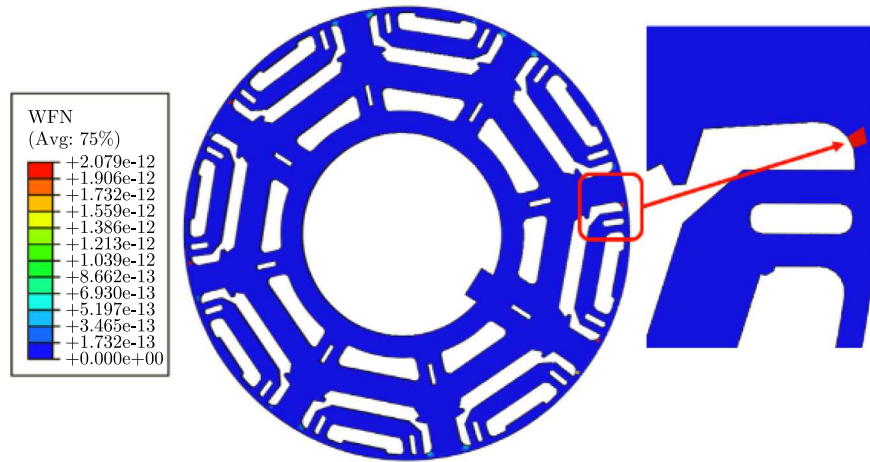Fig. 17. Volume fraction of holes caused by hole growth

Fig. 18. Pore volume fraction caused by pore nucleation

The hole evolution includes the growth of initial holes and the nucleation of secondary holes, but although the plastic deformation produced by the rotor at the peak condition is still small, as shown in Fig. 17, the volume fraction of holes caused by the growth of holes is $2.150 \cdot 10^{-6}$. In Fig. 18, the change in the volume fraction of holes caused by the nucleation of holes is only $2.079 \cdot 10^{-12}$. Therefore, the increase of the hole volume fraction of the rotor material under the peak condition is mainly caused by the growth of the initial holes, and the change caused by the nucleation of the secondary holes is smaller.

5. Conclusion

- The finite element inverse calibration method combined with the material tensile test at room temperature was used to calibrate the fine damage parameters of the GTN model of a silicon steel material at room temperature. On this basis, the damage parameters of the GTN model of silicon steel at 70°C, 100°C and 150°C were finally fitted by considering the influence of temperature on the model nucleation parameters combined with the material tensile test at high temperatures.
- Under the rated operating condition of the motor, the stress is mainly concentrated at the connection between the rotor and the shaft, and there is no significant stress concentration at the isolation bridge. The rotor does not reach the material yield limit, and there is no plastic strain, so the holes inside the material do not change, and the value is still the initial hole volume fraction.
- When the motor is in the peak operating condition, the centrifugal force acting on the rotor increases further, the stress is mainly concentrated at the connection between the spacer bridge and the pole shoe, and the corresponding plastic deformation occurs at the concentration point, and the volume fraction of the holes inside the material changes, but it is mainly caused by the growth of the initial holes.

References

1. Ahn J.H., Cheol H., Kim C.W., Choi J.Y., 2017, Rotor design of high-speed permanent magnet synchronous motors considering rotor magnet and sleeve materials, *IEEE Transactions on Applied Superconductivity*, **29**, 3, 1-4

2. Binder A., Schneider T., Klohr M., 2005, Fixation of buried and surface-mounted magnets in high-speed permanent-magnet synchronous machines, *IEEE Transactions on Industry Applications*, **42**, 4, 1031-1037

3. Dong J.P., Wang S.L., Zhou J., Yang B., Ma C., 2021, Study of ductile fracture criterion for stainless steel pipe shear process based on modified GTN model, *Engineering Mechanics*, **38**, 3, 239-247

4. Fang J., Qiu B.W., Yuan Z.X., 2020, Three-point bending crack expansion test and finite element simulation of X80 steel, *Weapon Materials Science and Engineering*, **43**, 3, 99-103

5. Feng C., Yi L., Liang P., Pei Y., 2016, Calculation of the maximum mechanical stress on the rotor of interior permanent-magnet synchronous motors, *IEEE Transactions on Industrial Electronics*, **63**, 6, 3420-3432

6. Gao Q.X., Wang X.L., Ding Q., 2021, Rotor strength analysis and structure design of ultra-high speed miniature permanent magnet motor, *Proceedings of the CSEE*, **41**, 8, 2856-2867

7. Gerada D., Mebarki A., Brown N.L., Gerada C., Cavagnino Andrea, Boglietti A., 2013, High-speed electrical machines: technologies, trends, and developments, *IEEE Transactions on Industrial Electronics*, **61**, 6, 2946-2959

8. Gurson A.L., 1977, Continuum theory of ductile rupture by void nucleation and growth. Part I. Yield criteria and flow rules for porous ductile media, *Journal of Engineering Materials and Technology*, **99**, 2-15

9. He L.G., Shi W.J., 2020, Temperature characteristics of vehicle motors under extreme variable working conditions, *Journal of Power Electronics*, **21**, 376-383

10. He L.G., Shi W., Xia X., Wu X.Y., Chen H.L„ Yan X., 2021, Research on temperature rise characteristics of vehicle motors under bench working condition, *Journal of Electrical Engineering and Technology*, **16**, 6, 3135-3143

11. Huang R., 2016, Study on the damage of creeping iron cylinder head based on fine view GTN model, Master's Thesis, Beijing University of Technology

12. Lee J., Jong Bong H., Park H., Kim D., 2022, Micromechanics-based modeling of plastic and ductile fracture of aluminum alloy 2024-O, *Engineering Fracture Mechanics*, **261**, 108-213

13. Li G., Cui S., 2020, Meso-mechanics and damage evolution of AA5182-O aluminum alloy sheet based on the GTN model, *Engineering Fracture Mechanics*, **235**, 107162

14. Li Y., Pei Y., Liang P., Chai F., 2014, Analysis of the rotor mechanical strength of interior permanent magnet synchronous in-wheel motor with high speed and large torque, *Transportation Electrification Asia-Pacific, IEEE*

15. Liang Q., Wang X., Chen X., Wang Y., 2011, 3 Dimensional finite element analysis of vehicle permanent magnet motor's rotor, *International Conference on Mechatronic Science, IEEE*

16. Liu Z., Han X.Y., Gao J., 2021, Analysis of rotor strength of high-speed permanent magnet motor based on thermo-structure coupling, *Electric Technology*, **22**, 5, 1-5+101

17. Mobasher M.E., Taylor P., Woelke P.B., Fleck N.A., Hutchinson J.W., Zhong A., 2022, Modeling the anchoring and performance of downhole equipment using an extended Gurson model, *Engineering Fracture Mechanics*, **261**, 108232

18. NEEDLEMAN A., TVERGAARD V., 1984, An analysis of ductile rupture in notched bars, *Journal of the Mechanics and Physics of Solids*, **32**, 6, 461-490

19. NIOI M., PINNA C., CELOTTO S., SWART E., FARRUGIA D., HUSAIN Z., GHADBEIGI H., 2019, Finite element modelling of surface defect evolution during hot rolling of silicon steel, *Journal of Materials Processing Technology*, **268**, 181-191

20. SHAO Y., WANG X., GAO Q., LI Y., 2019, Rotor strength analysis of ultra-high speed permanent magnet synchronous motor, *2019 22nd International Conference on Electrical Machines and Systems (ICEMS)*

21. SUN Q., YAN Y.X., CHEN J.J., 2013, Prediction of edge cracking during cold rolling of thin silicon steel plates containing edge defects based on GTN damage model, *Mechanical Engineering Materials*, **37**, 1, 93-97

22. TENCONI A., VASCHETTO S., VIGLIANI A., 2013, Electrical machines for high-speed applications: design considerations and tradeoffs, *IEEE Transactions on Industrial Electronics*, **61**, 6, 3022-3029

23. TVERGAARD V., NEEDLEMAN A., 1984, Analysis of the cup-cone fracture in a round tensile bar, *Acta Metallurgica*, **32**, 1, 157-169

24. XIE J.P., HU Q.C., MAI Q.L., 2019, Dynamic analysis and structure optimization of high-speed v-shaped permanent magnet rotor, *Micro and Special Electric Machines*, **47**, 5, 1-5+11

25. XU M.M., LIU G.J., CHEN Q., ZHAO W.X., 2019, Review on design and key technology development of permanent magnet assisted synchronous reluctance motor, *Proceedings of the CSEE*, **39**, 23, 7033-7043+7116

26. YAN Y., SUN Q., CHEN J., PAN H., 2013, The initiation and propagation of edge cracks of silicon steel during tandem cold rolling process based on the Gurson-Tvergaard-Needleman damage model, *Journal of Materials Processing Technology*, **4**, 598-605

27. ZHANG C., ZHU J.G., TONG W.M., 2017, Analysis and design of high-speed built-in permanent magnet rotor strength, *Journal of Electrical Machines and Control*, **21**, 12, 43-50

28. ZHANG F., DU G., WANG T., WANG F., CAO W., KIRTLEY J.L., 2016, Electromagnetic design and loss calculations of a 1.12-MW high-speed permanent-magnet motor for compressor applications, *IEEE Transactions on Energy Conversion*, **31**, 1, 132-140

29. ZHU Y., HU X.F., SONG M.C., 2021, Rotor strength analysis of high-speed permanent magnet motor, *Machine Tool and Hydraulics*, **49**, 6, 142-146+70